Brazilian Journal of Physics
ISSN: 0103-9733
luizno.bjp@gmail.com
Sociedade Brasileira de Física
Brasil

Nakahata, Masayuki
Neutrino Physics (Rapporteur talk)
Brazilian Journal of Physics, vol. 44, núm. 5, 2014, pp. 465-482
Sociedade Brasileira de Física
Sâo Paulo, Brasil

Braz J Phys (2014) 44:465–482
DOI 10.1007/s13538-014-0228-4

SOCIEDADE BRASILEIRA DE FÍSICA

PARTICLES AND FIELDS

Neutrino Physics (Rapporteur talk)

Masayuki Nakahata

Received: 28 April 2014 / Published online: 31 May 2014

Abstract Papers related to neutrino physics, submitted in the categories NU-EX (experimental results), NU-IN (methods, techniques, and instrumentation) and NU-TH (theory, model, and simulations) are reviewed with a brief introduction on the current understanding of neutrino masses and mixings.

Keywords Neutrino

1 Introduction

The categories NU-EX, NU-IN, and NU-TH at ICRC2013 cover neutrino physics over a wide energy range. As shown in Fig. 1, neutrino sources include solar neutrinos with energies of several megaelectronvolt, supernova burst neutrinos with energies of a few tens of MeV, atmospheric neutrinos with energies from a few hundred megaelectronvolt to a petaelectronvolt, and high-energy astrophysical neutrinos with energies of several teraelectronvolt or more.

The number of papers submitted to the various categories are 1 for solar neutrinos, 5 for supernova neutrinos, 13 for atmospheric neutrinos, 64 for high-energy astrophysical neutrinos, and 5 for other topics. So, a total of 88 papers were submitted, and all of them are impressive in one way or another. But, since it is impossible to cover all of them in this short rapporteur report, only papers that have notable results have been selected.

M. Nakahata (✉)
Kamioka Observatory, Institute for Cosmic Ray Research,
University of Tokyo, Tokyo, Japan
e-mail: nakahata@icrr.u-tokyo.ac.jp

M. Nakahata
Kavli Institute for the Physics and Mathematics
of the Universe (WPI), University of Tokyo, Tokyo, Japan

2 Neutrino Masses and Mixings

Before discussing the contributed papers at ICRC2013, our current understanding of neutrino masses and mixings will be described. The relation between the mass eigenstates (ν_1, ν_2, and ν_3) and the weak interaction (flavor) eigenstates (ν_e, ν_μ, and ν_τ) can be written:

$$\begin{pmatrix} \nu_e \\ \nu_\mu \\ \nu_\tau \end{pmatrix} = \begin{pmatrix} U_{e1} & U_{e2} & U_{e3} \\ U_{\mu 1} & U_{\mu 2} & U_{\mu 3} \\ U_{\tau 1} & U_{\tau 2} & U_{\tau 3} \end{pmatrix} \begin{pmatrix} \nu_1 \\ \nu_2 \\ \nu_3 \end{pmatrix}.$$

The unitary matrix U, which is referred to as the Pontecorvo-Maki-Nakagawa-Sakata (PMNS) matrix, can be decomposed into three mixing angles (θ_{12}, θ_{23}, θ_{13}) and one Charge conjugation Parity (CP) phase (δ) as follows:

$$\begin{pmatrix} 1 & 0 & 0 \\ 0 & c_{23} & s_{23} \\ 0 & -s_{23} & c_{23} \end{pmatrix} \begin{pmatrix} c_{13} & 0 & s_{13}e^{i\delta} \\ 0 & 1 & 0 \\ -s_{13}e^{-i\delta} & 0 & c_{13} \end{pmatrix} \begin{pmatrix} c_{21} & s_{12} & 0 \\ -s_{12} & c_{12} & 0 \\ 0 & 0 & 1 \end{pmatrix}$$

where $c_{ij} \equiv \cos\theta_{ij}$ and $s_{ij} \equiv \sin\theta_{ij}$. The general expression for the neutrino oscillation probability in a vacuum, $P(\nu_\alpha \to \nu_\beta; L)$, is

$$\delta_{\alpha\beta} - 4\sum_{j<k} \mathrm{Re}\left(U_{\alpha j}U^*_{\beta j}U^*_{\alpha k}U_{\beta k}\right)\sin^2\left(\frac{\Delta m^2_{jk}L}{4E}\right) + 2\sum_{j<k} \mathrm{Im}\left(U_{\alpha j}U^*_{\beta j}U^*_{\alpha k}U_{\beta k}\right)\sin\left(\frac{\Delta m^2_{jk}L}{2E}\right),$$

where $\Delta m^2_{jk} \equiv m^2_j - m^2_k$.

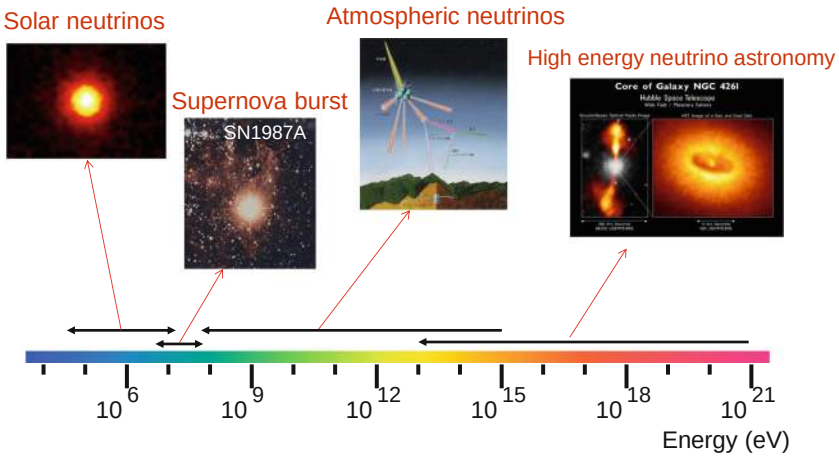

Fig. 1 Energy range covered by neutrino physics

The value of $\sin^2(2\theta_{23})$ and the absolute value of Δm^2_{32} have been measured using atmospheric and accelerator neutrinos, and the resulting contours are shown in Fig. 2.

The value of $\sin^2(2\theta_{23})$ is close to unity and $|\Delta m^2_{32}|$ is about $2.4 \times 10^{-3} eV^2$. The sign of Δm^2_{32} is not yet known; a positive sign is referred to as *normal* and a negative sign is referred to as *inverted*. $\sin^2(2\theta_{12})$ and Δm^2_{21} were measured using solar neutrinos and in a long baseline reactor experiment (KamLAND), and the resulting contours are shown in Fig. 3.

$\sin^2(\theta_{12})$ is 0.304 ± 0.013 and Δm^2_{21} is $7.45^{+0.20}_{-0.19} \times 10^{-5} eV^2$. Recently, θ_{13} was measured in accelerator experiments (T2K and MINOS) and short baseline reactor experiments (Daya Bay, RENO, and Double Chooz). A summary of the measured values is shown in Fig. 4.

Combining the results of the reactor experiments, $\sin^2(2\theta_{13})$ is 0.093 ± 0.009. So, we know now all three mixing angles and two independent values of Δm^2. As yet, unknown properties are the mass hierarchy, the CP phase δ, and the absolute value of neutrino masses. A graphical summary of known masses and mixings is shown in Fig. 5.

3 Solar Neutrinos

Solar neutrinos have been measured in the Homestake, Kamiokande, SAGE, GALLEX/GNO, Super-Kamiokande, SNO, KamLAND, and Borexino experiments. Figure 6 shows the ν_e survival probability ($P(\nu_e \rightarrow \nu_e)$) as a function of neutrino energy, determined by combining the results of these experiments [2].

The expected probability for neutrino oscillations, taking into account the Mikehev-Smirnov-Wolfenstein (MSW) effect, is also shown in the figure for the best-fit parameters from solar global and solar+KamLAND analyses. At ICRC2013, the latest results from the Super-Kamiokande were presented [2]. Because of the matter effect on neutrinos passing through the Earth, the flux at night is expected to be higher than that during the day. The results of the Super-Kamiokande observations indicated that the day/night asymmetry ($A_{DN} = (\Phi_{day} - \Phi_{night})/\frac{1}{2}(\Phi_{day} + \Phi_{night})$) is $-3.2 \pm 1.1 \pm 0.5$ %, and it is 2.7σ away from zero. Figure 7 shows the observed A_{DN} as a function of Δm^2_{21} together with the expected A_{DN}. The obtained

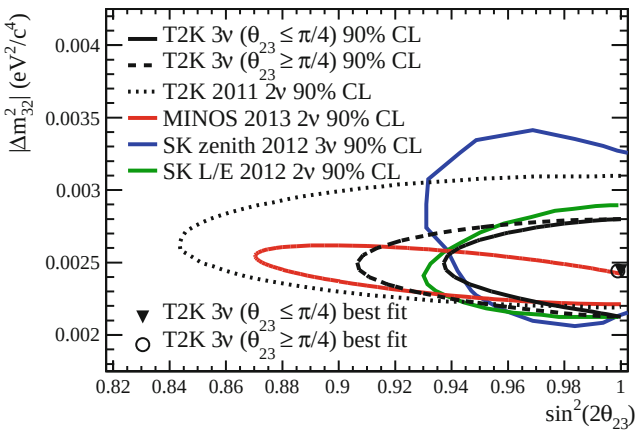

Fig. 2 Contours for $\sin^2(2\theta_{23})$ and the absolute value of Δm^2_{32} (from [1])

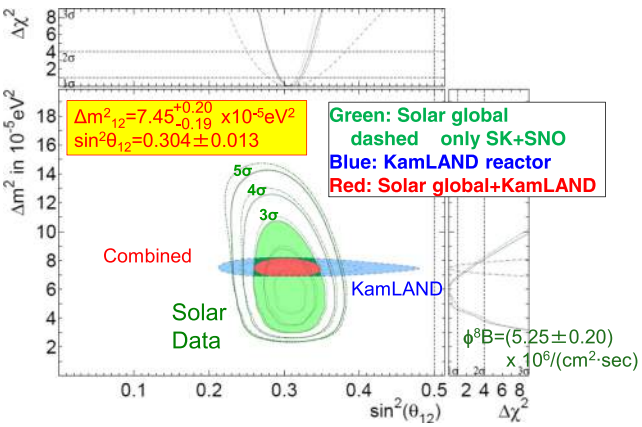

Fig. 3 Contours for $\sin^2(\theta_{12})$ and the absolute value of Δm^2_{21} from [2]

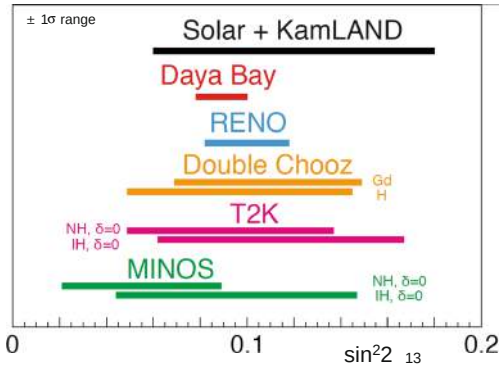

Fig. 4 Measured values of θ_{13}

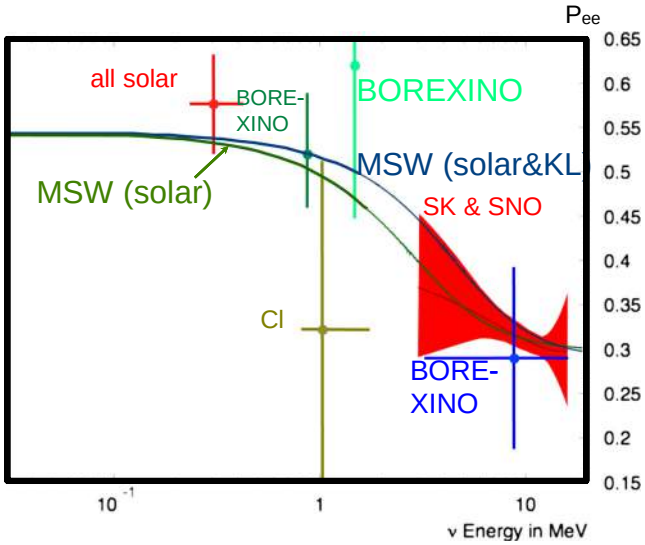

Fig. 6 ν_e survival probability determined by solar neutrino experiments [2]. Also shown are the expected probability curves considering the MSW effect for the best fit parameters obtained from solar global and solar+KamLAND analyses

A_{DN} is statistically consistent with the expectations for the Δm^2_{21} values obtained from the KamLAND and solar global analyses.

4 Supernova Neutrinos

Core collapse supernovae are the most energetic stellar phenomena in the universe. The total energy released by a core collapse is estimated to be $\sim 3 \times 10^{53}$erg, and 99 % of this energy is carried by neutrinos.

Figure 8 shows the history of underground detectors that are sensitive to galactic supernova bursts. The one with the longest operational history is the Baksan experiment, which is a 330 ton liquid scintillator detector located in the Baksan laboratory. Since no galactic supernova candidate has been found during the 28-year period from 1980 to 2013, this places an upper limit on the galactic supernova rate of $<$0.082/year at a 90 % confidence level (CL) [3]. The second longest running is the LVD experiment, which is a 1,000-ton liquid scintillator detector. LVD also found no supernova candidate and established an upper limit of $<$0.12/year at a 90 % CL [4]. Table 1 shows the list of currently operating supernova detectors and their sensitivity.

The Super-Kamiokande detector is able to detect several thousand supernova events for a galactic supernova, and it is possible to get directional information using neutrino-electron scattering events. The IceCube detector is capable of measuring the precise time profile of bursts containing many neutrino interaction events in ice. As a result of an

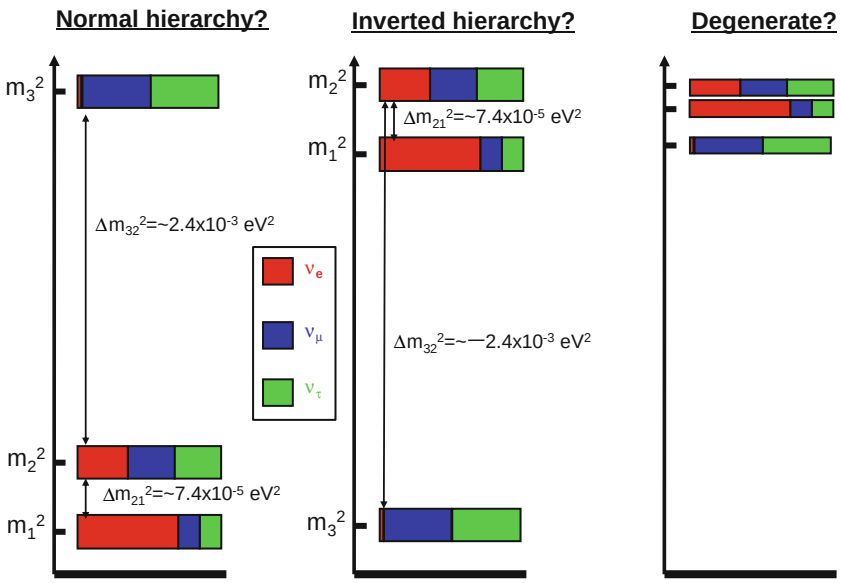

Fig. 5 Graphical summary of neutrino masses and mixings

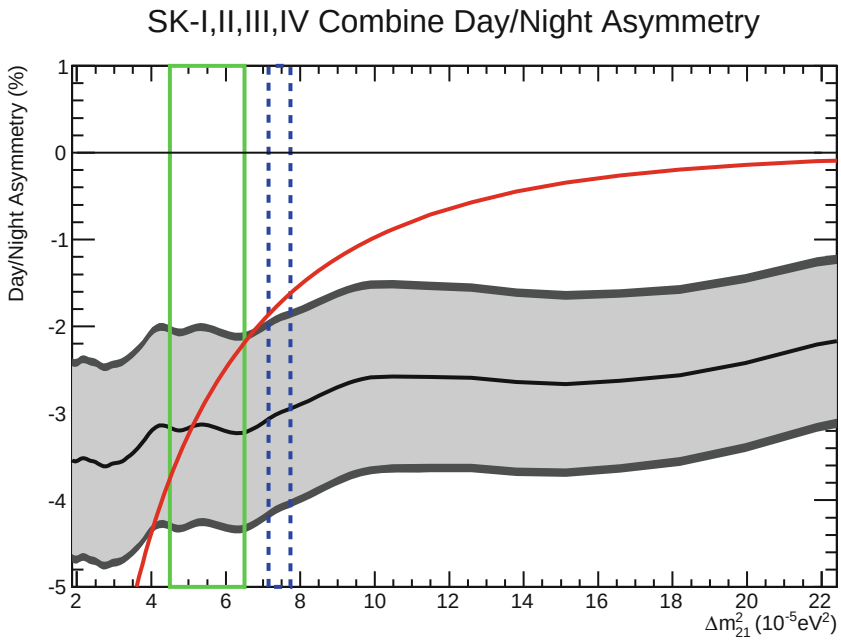

Fig. 7 Day/night flux asymmetry measured by Super-Kamiokande (*gray* band). Also shown are the expected asymmetry (*red*) and $\pm 1\sigma$ ranges of Δm^2_{21} from the solar global (*green*) and KamLAND (*blue*) analyses (from [2])

IceCube collaboration, an offline burst search of the data from April 2008 to May 2011 was reported in [5], and an improved data acquisition system that can record all hit information from -30 to $+60$ s was presented in [6]. This improvement enabled profiles to be recorded without the need for time binning (2-ms binning was previously required) and allowed the mean energy to be estimated by correlating the hits with an accuracy of $\sim$30 % for a supernova at a distance of 10 kpc.

Core-collapse supernovae have occurred throughout the universe since its beginning. For this reason, a diffuse neutrino background is expected to be present, that is associated with all the supernovae that have ever occurred; such neutrinos are referred to supernova relic neutrinos (SRNs). The expected SRN spectrums assuming some effective temperatures of the supernova burst are shown in Fig. 9 (left). $\bar{\nu}_e$ are expected to be the main neutrinos present in the energy window from 10 to 30 MeV. The interaction rate in the Super-Kamiokande detector is about 1.3–6.7 events/year. In order to tag neutrons produced by inverse beta interactions ($\bar{\nu}_e + p \rightarrow e^+ + n$), it is planned to dissolve 100 tons of a gadolinium compound in the detector, a project which is referred to as GADZOOKS!. Neutron capture by gadolinium produces a gamma ray cascade with an energy of 8 MeV (Fig. 9, right). Research and development concerning this project (called EGADS) was reported in [7].

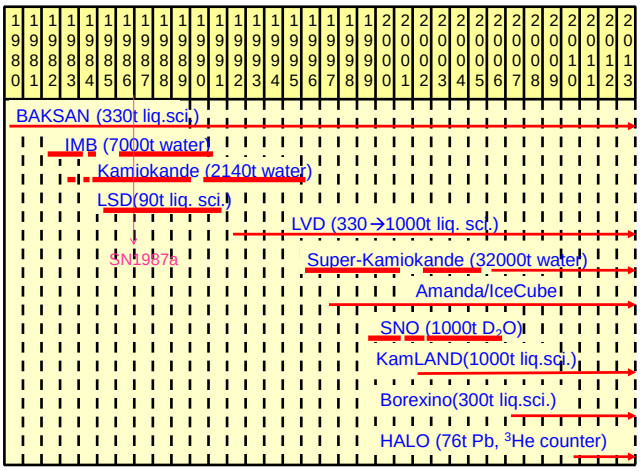

Fig. 8 History of underground detectors sensitive to galactic supernova bursts

5 Atmospheric Neutrinos

Atmospheric neutrinos are produced by cosmic ray interactions with atmospheric molecules, and both ν_μ and ν_e are created. At lower energy, the ratio of ν_μ and ν_e fluxes is almost 2. However, with increasing energy, this ratio also increases because high-energy muons reach the surface of the Earth before they decay. The deficit of upward-going atmospheric ν_μ observed by Super-Kamiokande was the first discovery of neutrino oscillations. Given their energy and traveling distance, which corresponds to the distance through the Earth, upward-going atmospheric neutrinos provide a convenient means of measuring θ_{23} and Δm^2_{32}. They can also be used to investigate the mass hierarchy due to the matter effect on neutrino oscillations.

Since θ_{13} has been precisely determined by short baseline reactor experiments, a neutrino oscillation analysis has

Table 1 Summary of current supernova experiments and expected signal for a supernova at a distance of 10 kpc. The possibility of obtaining directional information is indicated in the third column

Experiment	Detector description and expected supernova signal at 10 kpc	Directionality
Baksan (1980-)	330-ton liquid scintillator in 3,180 tanks.	No
	$\sim$100 $\bar{\nu}_e p \rightarrow e^+ n$ events.	
LVD (1992-)	1,000-ton liquid scintillator in 840 tanks.	No
	$\sim$300 $\bar{\nu}_e p \rightarrow e^+ n$ events.	
Super-Kamiokande (1996-)	32,000-ton water Cherenkov detector.	Yes
	$\sim$7300 $\bar{\nu}_e p \rightarrow e^+ n$ and $\sim$300 $\nu e \rightarrow \nu e$ events.	
KamLAND (2002-)	1,000 ton liquid scintillator, single volume.	No
	$\sim$300 $\bar{\nu}_e p \rightarrow e^+ n$, several tens of CC and NC events on ^{12}C,	
	and $\sim$300 $\nu p \rightarrow \nu p$ NC events.	
IceCube (2005-)	Gigaton ice target. Coherent increase of PMT single rates.	No
	Hit precision time profile measurement.	
Borexino (2007-)	300-ton liquid scintillator, single volume.	No
	$\sim$100 $\bar{\nu}_e p \rightarrow e^+ n$, a few tens CC and NC events on ^{12}C,	
	and $\sim$100 $\nu p \rightarrow \nu p$ NC events.	
HALO (2010-)	^{3}He neutron detectors with 76-ton lead target.	No
	$\sim$40 events expected.	

been performed at Super-Kamiokande by fixing the θ_{13} parameter. Figure 10 shows contours of $\sin^2\theta_{23}$ and Δm^2_{32}, where the left and right figures are for normal and inverted mass hierarchies, respectively.

The current data still allows full mixing ($\sin^2\theta_{23} = 0.5$) and both octants ($\sin^2\theta_{23} < 0.5$ and > 0.5). The CP phase δ and mass hierarchy can also be discussed based on the Super-Kamiokande data. The left panels in Fig. 11 show the allowed range for the CP phase δ for the normal and inverted mass hierarchies, and the right panel shows an overlay of the two hierarchies with vertical axis units of absolute χ^2. It can be seen that the inverted hierarchy is slightly preferred, with a χ^2 difference of 1.5.

The MINOS collaboration presented an oscillation analysis combining beam data and atmospheric neutrino data [8]. The advantage of the MINOS experiment is its ability to achieve charge separation, and it is possible to investigate neutrino and anti-neutrino oscillations separately. Figure 12 shows the Δm^2_{32} contour for neutrinos and anti-neutrinos; they are seen to be consistent with each other.

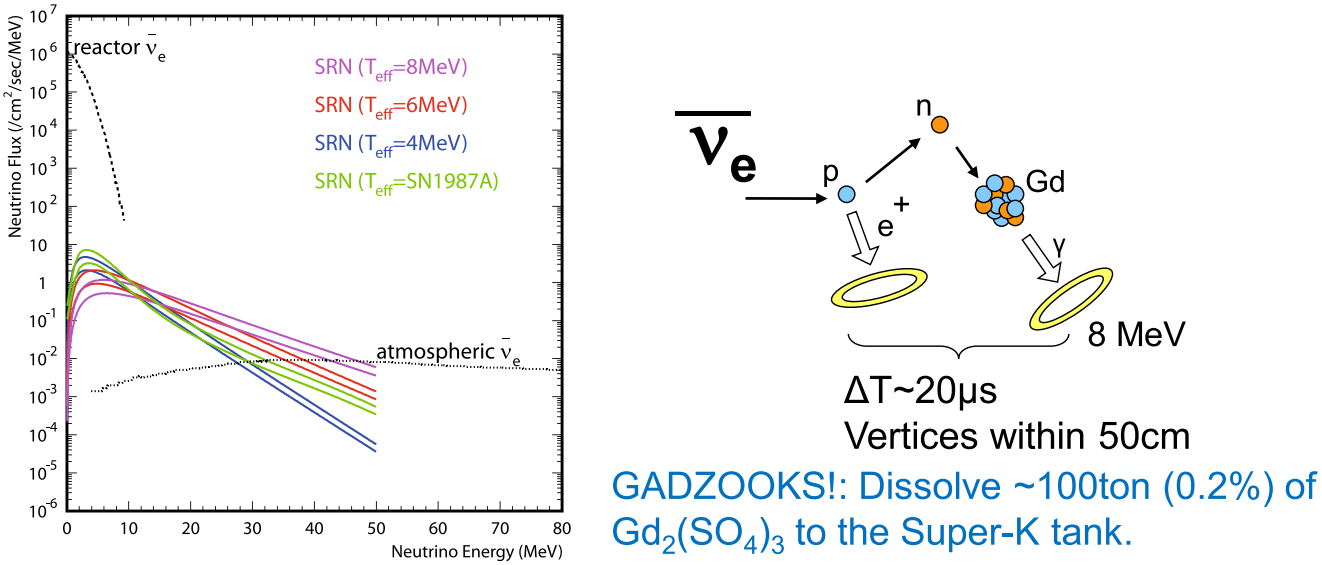

Fig. 9 (*left*) Predicted SRN spectrum for different neutrino temperatures. (*right*) Principle of SRN detection using gadolinium at Super-Kamiokande. Figures are from [7]

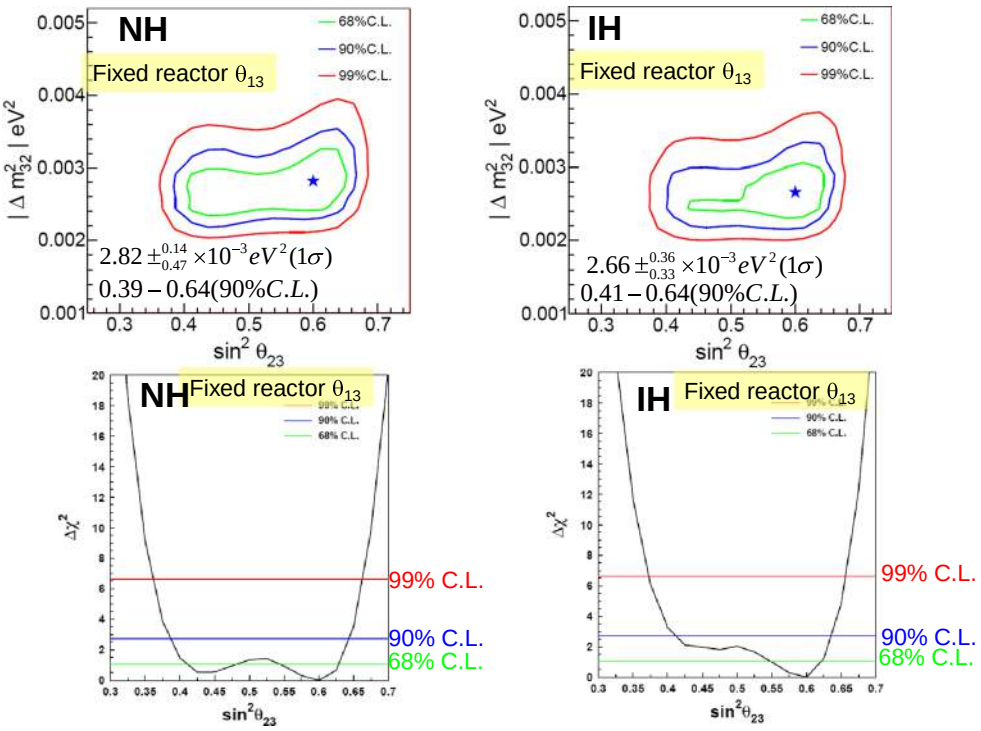

Fig. 10 Contours of $\sin^2\theta_{23}$ and Δm^2_{32} obtained from atmospheric neutrino analysis by Super-Kamiokande. The θ_{13} value is fixed based on the best fit to the results of short baseline reactor experiments. The left and right figures correspond to normal and inverted mass hierarchies, respectively

Based on the Earth's diameter of 12,700 km and the known Δm^2_{32} value, the maximum disappearance of ν_μ is expected at around 25 GeV. IceCube/DeepCore can detect events with such energy, and results on atmospheric neutrino oscillations are presented in [9] and [10]. Figure 13 shows the ratio of the number of observed events to the expected number as a function of the neutrino travel distance through the Earth (L_{osc}) divided by the reconstructed track length

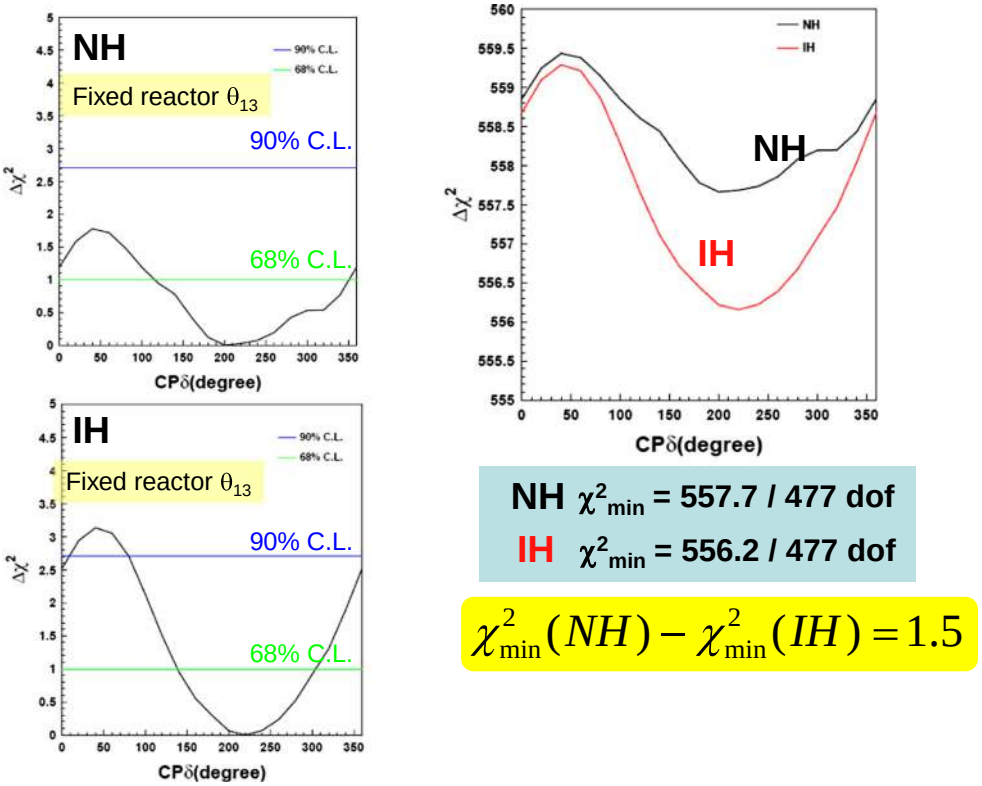

Fig. 11 (*Left*) $\Delta\chi^2$ as a function of CP δ based on Super-Kamiokande atmospheric neutrino data for the normal (*upper*) and inverted (*lower*) mass hierarchies. The θ_{13} value is fixed based on the best fit to the results of short baseline reactor experiments. (*Right*) Overlay of plots for normal and inverted hierarchies, with vertical axis units of absolute χ^2

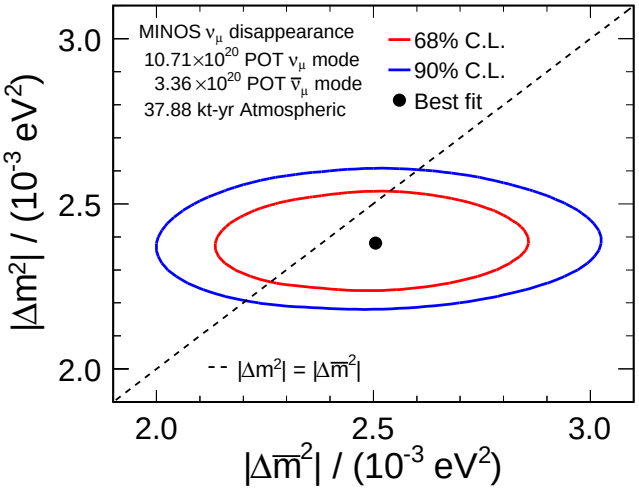

Fig. 12 Absolute value of Δm^2 for neutrinos (($|\Delta m^2|$) and anti-neutrinos ($|\Delta\overline{m}^2|$) obtained by analysis of MINOS beam and atmospheric data [8]

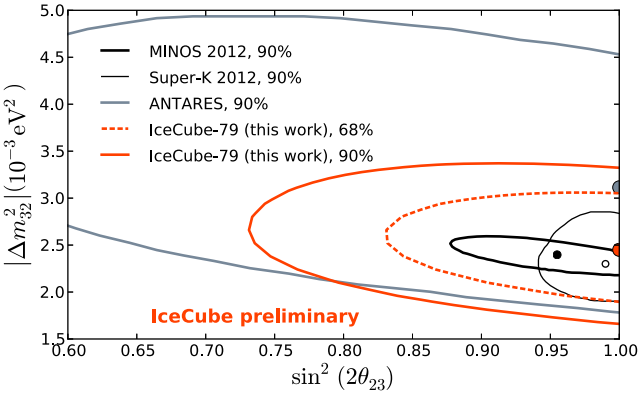

Fig. 14 Contours of neutrino oscillation parameters obtained by IceCube/DeepCore [9]

(l_{reco}). Since l_{reco} is proportional to neutrino energy, the horizontal axis corresponds to L/E. A deficit of events at the relevant L/E is clearly observed.

Figure 14 shows contours of the oscillation parameters obtained by IceCube/DeepCore.

As indicated by the Super-Kamiokande results shown above, it is possible to determine the mass hierarchy using atmospheric neutrinos. The ν_μ survival probability depends on whether the mass hierarchy is normal or inverted because of different matter effects on ν_μ and $\overline{\nu_\mu}$, and the fact that the ν_μ cross section is about three times larger than that of $\overline{\nu_\mu}$. However, a large target detector volume and a good angular resolution are necessary because the effect of the mass hierarchy is expected to be small. The PINGU project involves the deployment of a dense detector array at the IceCube/DeepCore site for a mass hierarchy measurement. A study on detector optimization (number of strings and their spacing) was reported in [11]. Figure 15 shows the sensitivity for mass hierarchy determination using 20 or 40 strings as a function of running time. A significance of 5σ can be achieved within 2–5 years.

An updated calculation of atmospheric neutrino fluxes was reported in [12]. The atmospheric neutrino flux depends on the atmospheric density, and the time averaged density from US-standard 76 has been used for these calculations so far. The NRLMSISE-00 atmospheric model gives density variations as a function of position on the Earth and the time of year. Using this information, the neutrino fluxes were recalculated for the Kamioka, INO and South Pole sites. Figure 16 shows the monthly flux variation at 10 TeV for

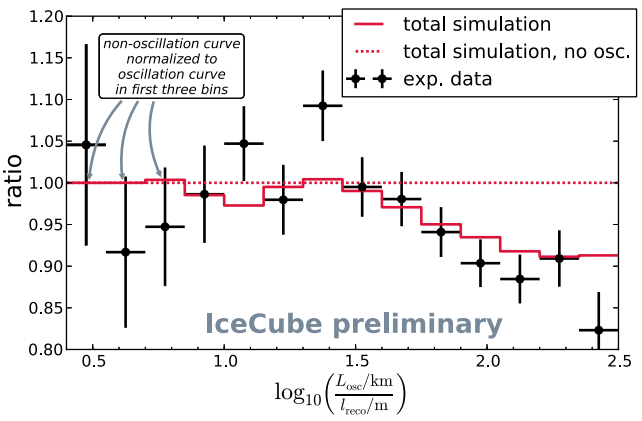

Fig. 13 Ratio between number of observed events and expected number against neutrino travel distance divided by reconstructed track length, based on IceCube/DeepCore data [9]

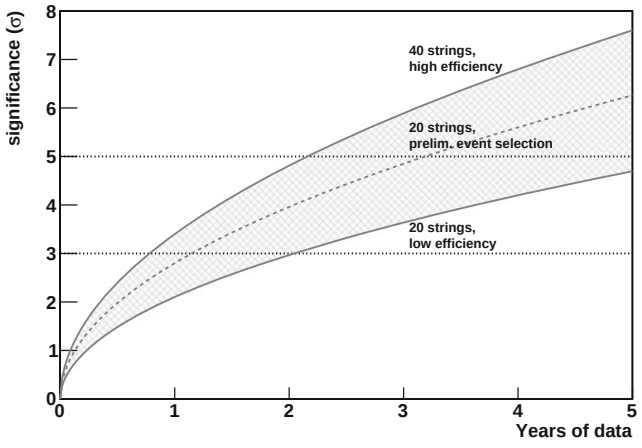

Fig. 15 Sensitivity of PINGU for mass hierarchy determination as a function of running time for different numbers of detector strings and efficiency levels [11]

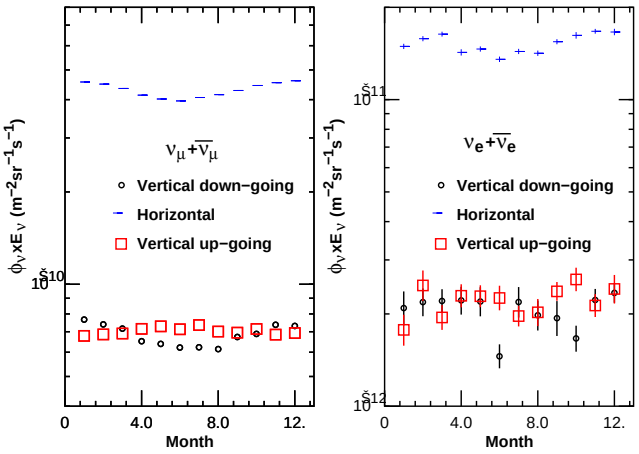

Fig. 16 Calculated atmospheric neutrino fluxes for $\nu_\mu + \overline{\nu_\mu}$ (*left*) and $\nu_e + \overline{\nu_e}$ (*right*) at 10 TeV at South Pole site (from [12])

the South Pole site. It can be seen that a seasonal variation is expected even at such higher energy.

In fact, the IceCube collaboration reported the observation of seasonal variations in [13]. Figure 17 shows the time variation of atmospheric neutrino events from April 2008 to July 2011 (data points in the figure). Events were selected in the zenith angle range of $90° < \theta < 120°$. A seasonal variation of about 5 % is seen with a statistical significance of about 3.4σ.

The spectrum of atmospheric neutrinos is a convolution of the primary spectrum of cosmic-ray nucleons with the spectrum of mesons and their decay products produced in the resulting cascade. Conventional spectrum calculations have considered only π and K mesons. Charmed mesons and baryons may contribute to the high-energy tail of the atmospheric neutrino spectrum, which is referred to as the "prompt component", and this topic was discussed in [14]. Figure 18 shows the calculated spectrum with the charm contribution included, where Sibyll2.2f was used for the event generator. The inclusion of the charm contribution leads to higher values for energies greater than ∼10 TeV for ν_e and greater than ∼100 TeV for ν_μ.

Similar conclusion was given by an independent study presented in [15]. The effect of the model used for the primary nucleon spectrum was studied in [14]. Figure 19 shows various models for the primary nucleon spectrum (left) and the ν_μ spectra calculated using these models (right). The results of the above studies make it clear that when calculating the ν_μ spectrum in the PeV energy range, precise knowledge of the charm contribution and the primary cosmic ray spectrum are essential.

6 High-Energy Neutrinos

High-energy neutrinos are important sources of information on cosmic rays. The sky has been observed using photons and hadrons. However, photons with energies above 10^{14} eV cannot travel more than 10 Mpc because of interactions with the cosmological diffuse infrared background and intergalactic matter. Protons with energies above 10^{20} eV cannot travel more than 50 Mpc due to Greisen-Zatsepin-Kuzmin (GZK) interactions. On the other hand, neutrinos essentially do not interact with matter and can be used as a probe for investigating distant regions of the universe at a wide range of energies. Neutrinos are electrically neutral particles and are insensitive to magnetic fields, so that the location of sources producing high-energy neutrinos can be identified. Although it is known that the majority of cosmic rays are hadrons, the actual origin of cosmic rays is still unclear. Hadron interactions in the cosmic accelerators must have produced neutrinos through $\pi^\pm$ production and if neutrinos from such sources are observed, it would reveal the origin of cosmic rays. One difficulty in observing neutrinos is that a very large detector mass is required because of the very small interaction cross section for neutrinos and matter. In order to detect high-energy neutrinos, a target mass on the order of cubic kilometers is required. At ICRC2013, there

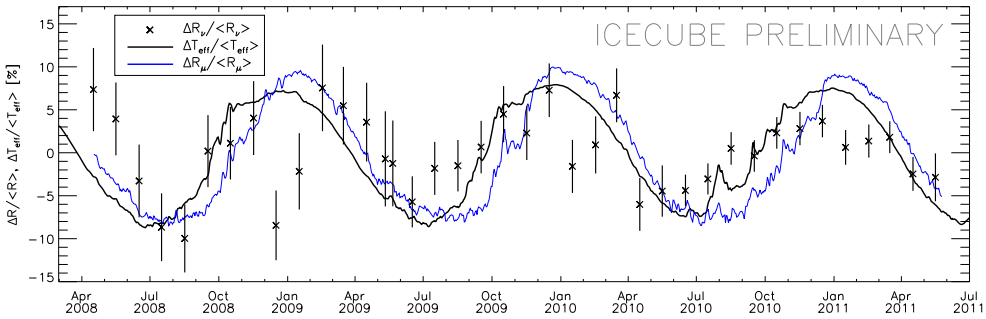

Fig. 17 Relative variation in monthly atmospheric neutrino rate at IceCube within the zenith angle range $90° < \theta < 120°$ between April 2008 and July 2011 (*bars* represent statistical errors). The *black curve* shows the effective temperature change in the region and the *blue curve* shows the rate of downward muon events during the same time period. (from [13])

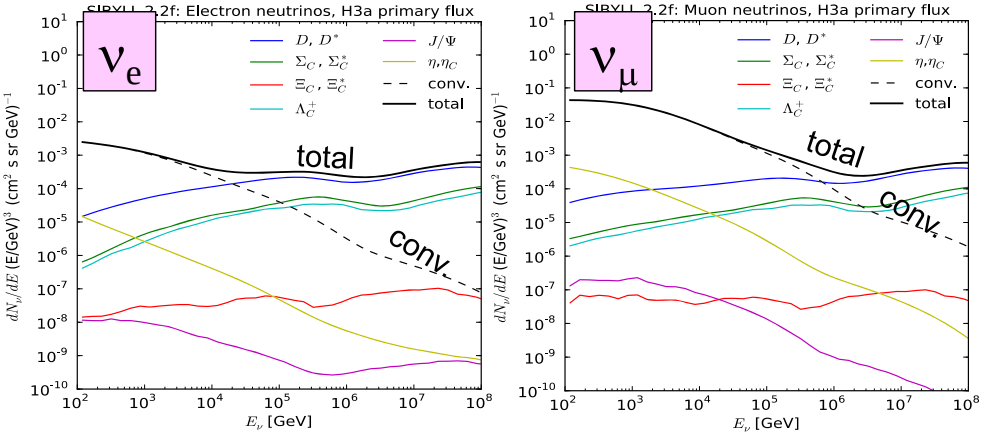

Fig. 18 Calculated atmospheric ν_e(*left*) and ν_μ spectra, with charm contribution included (from [14]). The *dashed curve* shows the results of conventional calculations, which consider only π and K mesons. The *colored curves* indicate the individual contributions from each charmed meson and baryon

were many contributions in the field of high-energy neutrinos. This is because of the large amount of physics results that have been obtained using the large high-energy neutrino detectors, IceCube and ANTARES. Schematic views of the IceCube and ANTARES detectors are shown in Fig. 20.

IceCube is located at the South Pole and the detector volume is about $(1\ km)^3$. A total of 5,160 optical modules are deployed in 86 strings at depths of 1,450–2,450 m beneath the ice surface. Even during its construction phase, measurements were being carried out, and the resulting datasets are referred to in terms of the number of detector strings that were in use at the time. IceCube-40, IceCube-59 and IceCube-79 refer to data obtained during the periods 2008–2009, 2009–2010, and 2010–2011, respectively. Measurements have been made with the full string set (IceCube-86) since 2011.

The ANTARES detector is located 2.5 km beneath the Mediterranean Sea off the coast of Toulon, France. A total of 885 optical modules are deployed in 12 strings, and the detector volume is 0.2 km×0.2 km×0.45 km. Construction of the detector was completed in 2008 and measurements have been ongoing since then.

One of the most important results presented at ICRC2013 was evidence for high-energy extraterrestrial neutrinos observed at IceCube [16]. IceCube-79 and −86 data taken during a period of 662 days from May 2010 to May 2012 were used for the analysis. The detector was subdivided into an inner region and an outer veto region, and events whose vertex was contained within the inner region were considered. These events were selected by a criterion of no earlier hits occurred in the veto region. Figure 21 shows the distribution of the total PMT charge (Q_{tot}) for the selected events. For $Q_{tot} > 6{,}000$ photoelectrons, 28 events were observed, and the estimated background was $10.6^{+5.0}_{-3.6}$. The uncertainty in the prompt component was estimated based on the upper limit obtained by analysis of IceCube-59 ν_μ data. The excess of events above the background has a statistical significance of about 4σ.

The energy and direction of the selected events were reconstructed, and Fig. 22 shows the energy vs. declination plot. Seven events are associated with muons (crosses), and

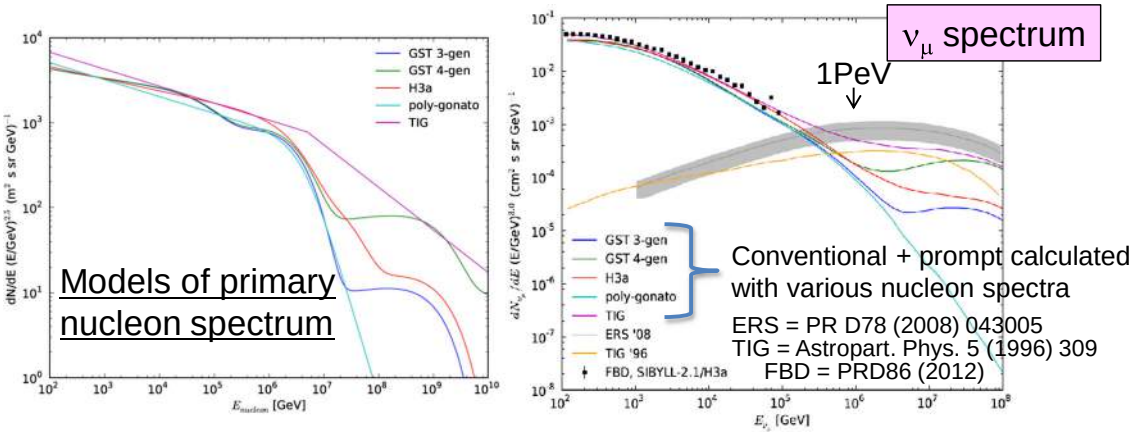

Fig. 19 Models for primary nucleon spectrum (*left*) and atmospheric ν_μ spectra calculated using these models (from [14])

Fig. 20 Schematic view of IceCube (*left*) and ANTARES (*right*)

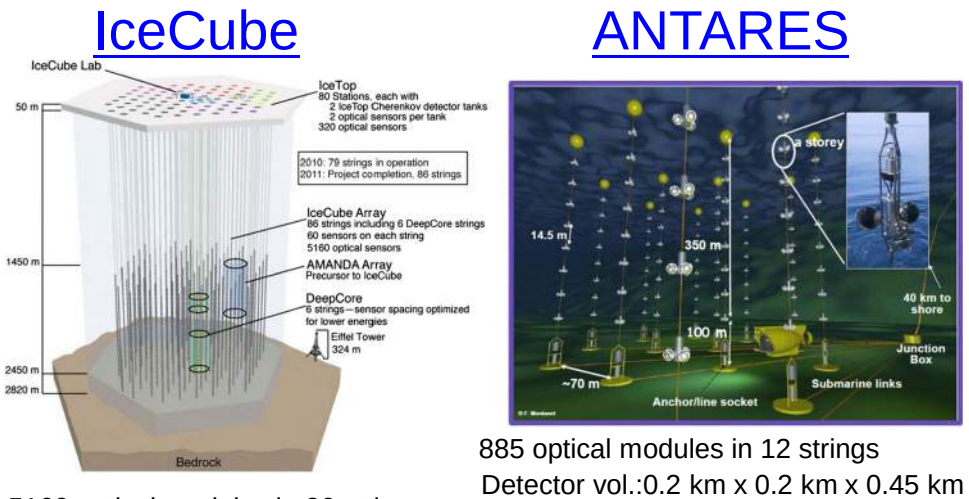

5160 optical modules in 86 strings

Detector volume: $(1\ \text{km})^3$

Data phases:

IceCube 40 (2008-9)
IceCube 59 (2009-10)
IceCube 79 (2010-11)
IceCube 86 (2011-)

885 optical modules in 12 strings

Detector vol.:0.2 km x 0.2 km x 0.45 km

Detector construction completed in 2008.

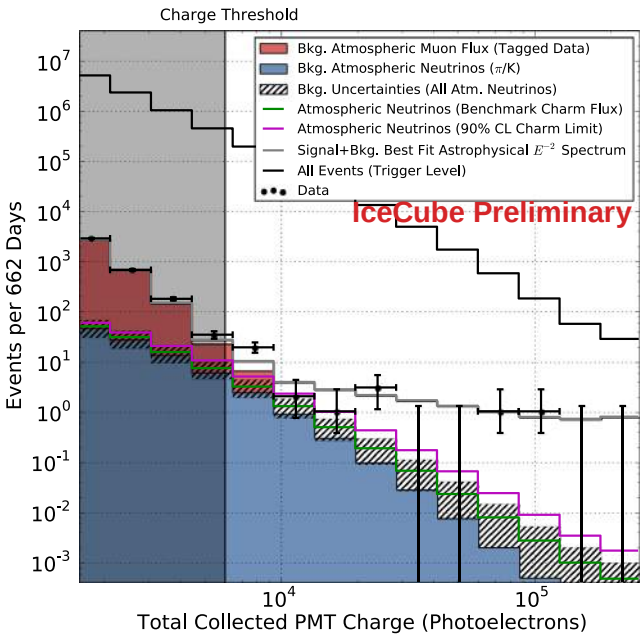

Fig. 21 Distribution of total PMT charge (Q_{tot}) for vertex-contained events at IceCube (data points with *error bars*) (from [16]). The muon background estimated from the data is indicated by the *red histogram*. The data points in the *unshaded region*, at $Q_{tot} > 6,000$, correspond to the events reported in this work. The atmospheric neutrino flux and its uncertainty are indicated by the *blue* and *black hatched histograms*, respectively. The *gray histogram* represents the best-fit astrophysical spectrum with an E^{-2} energy dependence

have an angular resolution of about 1°, while the remainder are due to either electromagnetic or hadronic showers (filled circles), and have an energy-dependent resolution of about 15°.

Figure 23 shows the energy spectrum together with the best-fit astrophysical spectrum with an E^{-2} energy dependence. The best-fit flux is given by $E^2\Phi_\nu(E) = (1.2 \pm 0.4) \times 10^{-8}\,\text{GeV}\,\text{cm}^{-2}\,\text{s}^{-1}\,\text{sr}^{-1}$ (per ν flavor). Since the spectrum does not extend above 2 TeV, it indicates a potential cutoff at about 2-5 TeV.

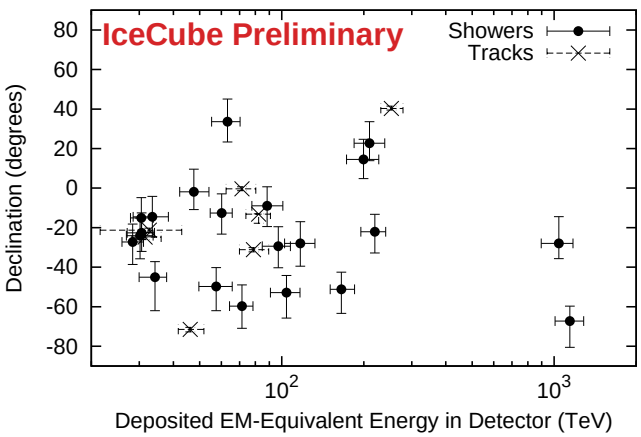

Fig. 22 Declination and best-fit deposited energy of the vertex-contained events at IceCube (from [16]). The *error bars* represent 68 % confidence intervals and include both statistical and systematic uncertainties. The *energies* shown represent the energy deposited in the detector assuming that all light emission is from electromagnetic showers

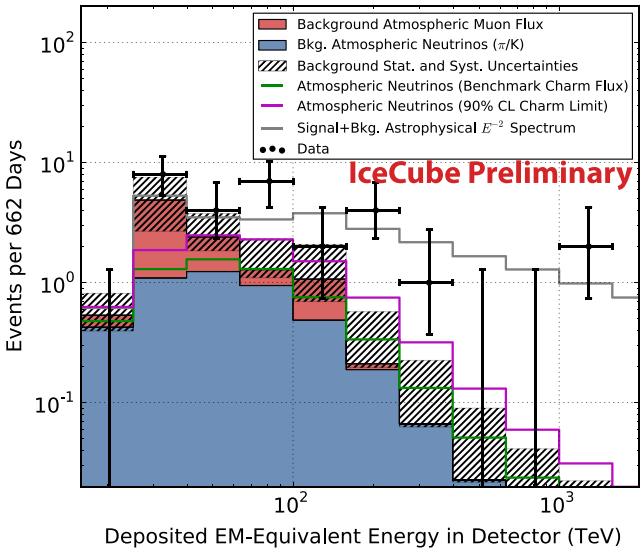

Fig. 23 Distribution of deposited energy of observed vertex-contained events at IceCube (from [16]). The estimated distribution of background atmospheric muons is shown in *red*. The combined statistical and systematic uncertainty for the sum of the backgrounds is indicated by the hatched area. The *green* and *magenta lines* represent specific charm levels for a benchmark theoretical model and the current experimental 90 % CL upper bound, respectively. The *gray line* shows the best-fit E^{-2} astrophysical spectrum with $E^2\Phi_\nu(E) = 1.2 \times 10^{-8}$ GeV cm^{-2} s^{-1} sr^{-1} (per flavor) assuming a (ν_e, ν_μ, ν_τ) ratio of (1:1:1)

Taking into account the angular resolution of the observed events, the degree of clustering was evaluated, and the results are shown in Fig. 24. The most significant clustering for all events had a p value of 80 %, and for shower events, the p value was 8 %. Thus, more measurement data are necessary before event clustering can be discussed.

Based on 4 years of data from the IceCube-40, -59, -79, and -86 data sets, an investigation into the correlation between neutrino events and gamma-ray bursts (GRBs) was reported in [17]. The up-going ν_μ channel was selected for this analysis, and horizontal events with declinations between 0 and $-5°$ were included because the ice cap itself provides a sufficient overburden to attenuate the cosmic ray muon background. The up-going ν_μ channel has a high angular resolution of 1° at 3 TeV and 0.5° at 1 PeV. A total of 543 GRBs were observed at declinations greater than $-5°$ during the search period. The search window was determined by the time of the gamma-ray emission and the location of each burst in the sky. Only one coincidence candidate (GRB100718B) remained after the selection, but its significance was not large (pre-trial p value of 0.11 or 1.2σ). The upper limit for the GRB flux is shown in Fig. 25 as a function of the first break energy (ε_b), which is defined as $\Phi_\nu \cdot \{E^{-1}/\varepsilon_b, E < \varepsilon_b;\ E^{-2}, \varepsilon_b \leq E\}$.

As shown in the figure, the upper limit is below the predictions of models that assume that the highest energy cosmic rays are from GRBs. Thus, the IceCube results falsified this hypothesis.

The ANTARES collaboration also reported an analysis of the correlation between neutrino events and GRBs in [18]. A total of 296 GRBs were observed from December 2007 to December 2011. ANTARES events were selected that occurred within the observed GRB period ($\sim$ 1 min/GRB), and whose reconstructed direction was within 10° of the GRB direction. Also, quality cuts were applied to exclude down-going cosmic ray muons, and an extended maximum likelihood analysis was carried out to exclude the background. The results yielded no suitable coincidence events so that the flux upper limits shown in Fig. 26 were obtained.

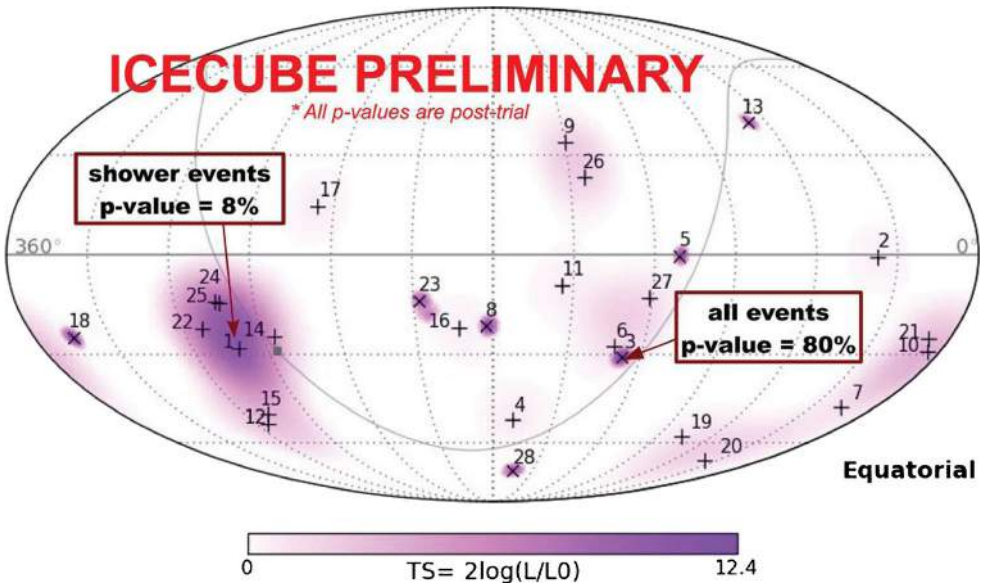

Fig. 24 Sky map for observed vertex-contained events at IceCube (from [16]). *Plus marks* indicate electromagnetic or hadronic shower events and *crosses* indicate muons

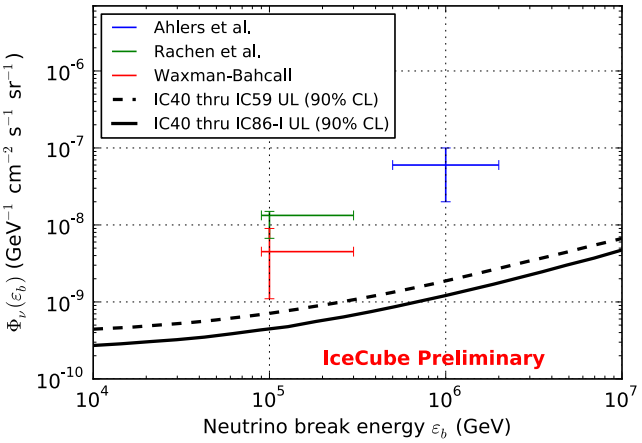

Fig. 25 90 % CL upper limits from published IC40+IC59 analysis (*dashed curve*) and the reported 4-year analysis (*solid curve*) (from [17]). Also shown are predictions of the models of Ahleres et al., Rachen et al., and the Waxman-Bahcall model. These models assume that the highest energy cosmic rays are from GRBs

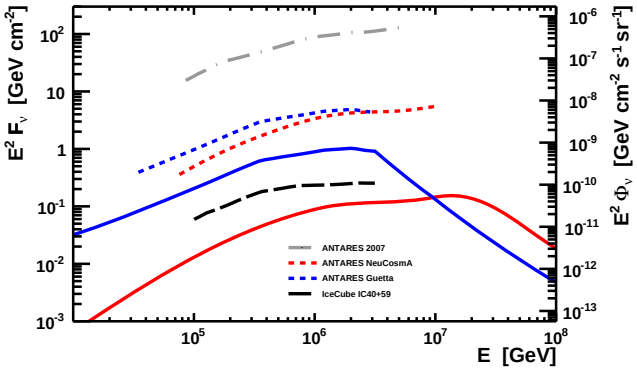

Fig. 26 Comparison of 90 % confidence limits (*dashed*) with expected fluxes (*solid*) for the GRB analysis by ANTARES (from [18]). The vertical axis shows summed $\nu_\mu + \bar{\nu}_\mu$ spectra of the 296 GRBs used in this analysis, using the NeuCosmA (*red*) and 'two-break' Guetta (*blue*) models

A search for point and extended sources at IceCube was reported in [19]. A total of 1,371 days of data from the IceCube-40, -59, and -79 data sets and the first year of the IceCube-86 data set were used in the analysis. After applying various cuts to remove atmospheric muons from cosmic rays, 394,000 events remained as shown in Fig. 27. A total of 178,000 neutrino candidates were observed in the northern sky, which were almost pure up-going atmospheric neutrinos. This was still valid up to 5° above the horizon. Above 5°, the data were dominated by high-energy atmospheric muon bundles, which closely mimic neutrinos.

In the all-sky scan, the region with the most significant deviation in the northern sky was located at 11.45° r.a. and 31.35° dec., and had a post-trial probability (the fraction of scrambled sky maps with at least one spot with an equal or higher significance for each region of the sky) of 38 %. For the southern sky, the most significant deviation was at 296.95° r.a. and −75.75° dec., and had a post-trial probability of 9 %. Thus, these results are consistent with the background-only hypothesis.

A point source search at ANTARES was reported in [20]. A total of 1,339 days of data from 2007 to 2012 were analyzed. Events were reconstructed using the time and position information of the corresponding hits and only events with upward-going tracks were selected. Applying further cuts on reconstruction quality, zenith angle, and estimated angular resolution, 5,516 neutrino candidates were selected. Based on a Monte Carlo estimation, 90 % of the sample should correspond to atmospheric neutrinos. The resulting sky map of neutrino candidates is shown in Fig. 28.

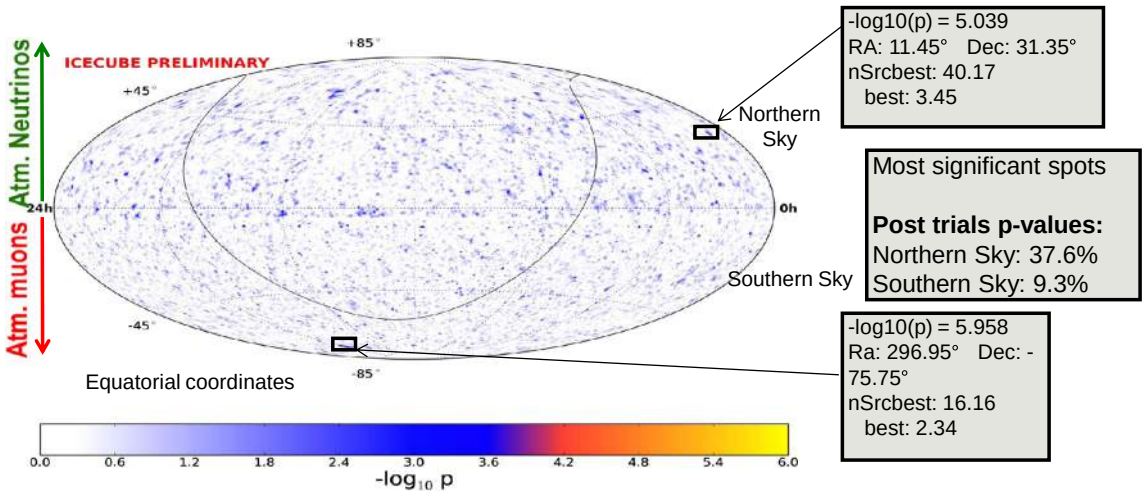

Fig. 27 Sky map obtained from 4 years of IceCube data (from [19])

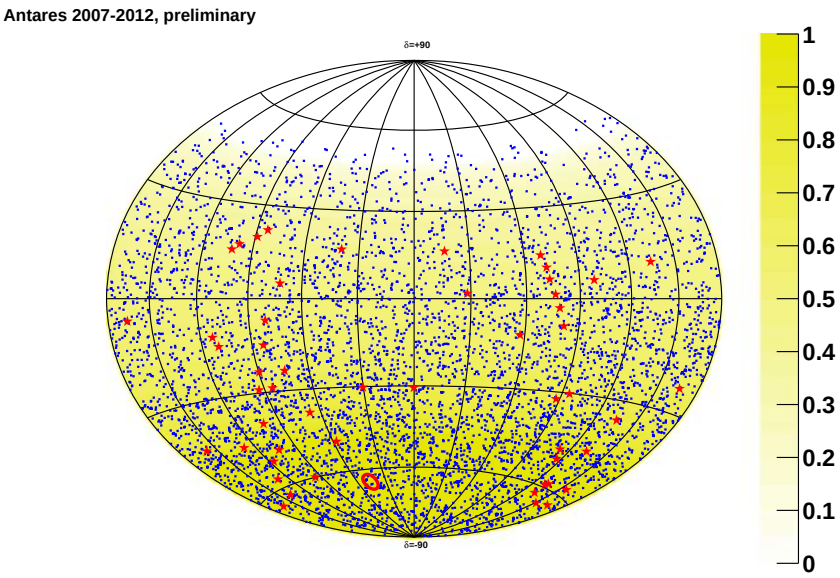

Fig. 28 Sky map obtained from 1,339 days of ANTARES data (from [20]). The position of the most significant cluster is indicated by the *circle*. The stars denote the position of the 50 possible neutrino sources

The most significant cluster was found at $(\alpha_i, \delta_i) = (-47.8°, -64.9°)$, and contained 14 events within a 2° search cone. The estimated background was 6.3, so this corresponds to a p value of 2.1 %. Searches for possible neutrino sources were also conducted but no significant excess was observed yet. Figure 29 shows the upper flux limits for these sources.

Specific source-related searches were also reported at ICRC2013. From the IceCube collaboration, neutrinos from the Cygnus region [21], multi-flare AGNs [22] and flaring and periodic sources [23] were reported. In the ANTARES collaboration, the coincidence of neutrinos and gravitational waves [24], gamma-ray flaring blazars [25], Fermi bubbles [26], and gravitational lensing sources [27] was investigated, and a 2-point correlation analysis [28] was reported. Although no significant excesses were identified, the sensitivity will soon reach interesting flux levels.

Some interesting detection possibilities at IceCube were reported. High-energy tau neutrinos (ν_τ) may produce two showers in the IceCube detector and yield a double-pulse time sequence. Feasibility and the effectiveness of various background rejection methods was discussed in [29], and 0.32 ± 0.04 events/year of ν_τ charged current events are expected assuming a flux of all neutrino flavors of $E^2 \Phi_\nu(E) = 3.6 \times 10^{-8}\,\mathrm{GeV\,cm^{-2}\,s^{-1}\,sr^{-1}}$. Due to the Glashow resonance ($\bar{\nu}_e + e^- \rightarrow W^-$), an event excess at

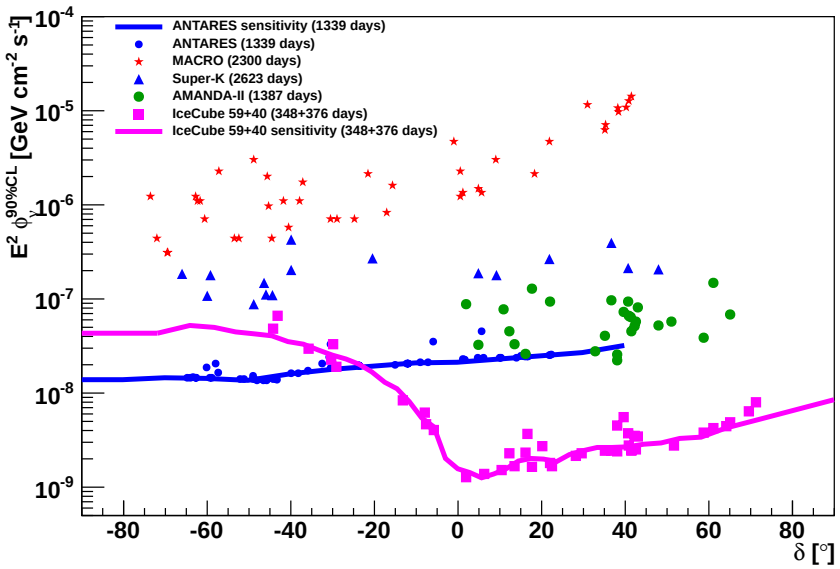

Fig. 29 (from [20]) *Blue symbols* indicate upper flux limits for possible neutrino sources assuming a E_ν^{-2} spectral shape. The *blue curve* represents the sensitivity, which is defined as the median expected limit. Several previously published limits for sources in both the southern and northern sky are also shown

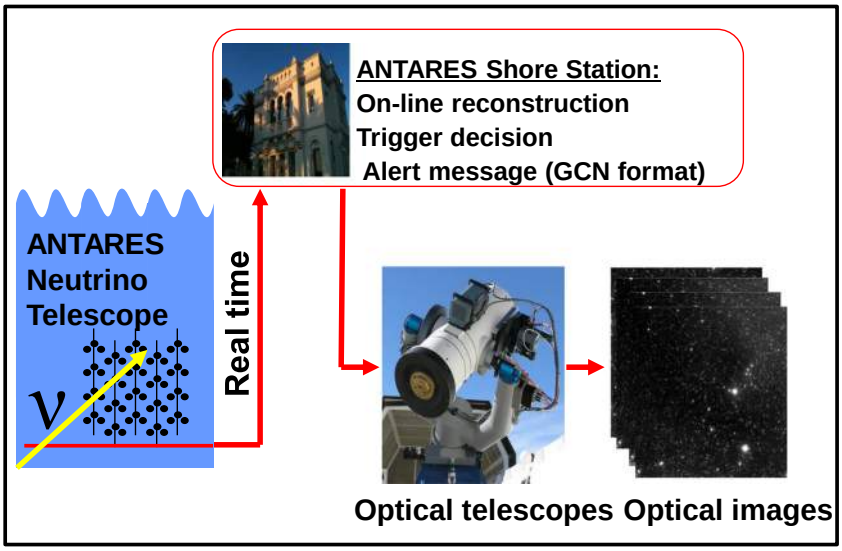

Fig. 30 TAToO alert system at ANTARES (from [31])

$E_\nu =\sim 6.3 PeV$ is expected [30]. The number of expected excess events is 0.9(0.4) events/year from $pp(p\gamma)$ sources for $5 PeV < E_{vis} < 7 PeV$ assuming electron type neutrino flux of $E^2\Phi(\nu_e + \bar{\nu_e}) = 1 \times 10^{-8}\,\mathrm{GeV\,cm^{-2}\,s^{-1}\,sr^{-1}}$.

Neutrino detectors monitor the whole sky (or half the sky if only upward-going events are selected) all of the time. However, optical, x-ray, and gamma-ray telescopes can monitor only a limited field of view. For transient sources such as GRBs and supernovae, this presents a problem because it may not be possible to carry out observations fast enough to capture such events. In order to overcome this problem, rapid analysis systems for neutrino events have been implemented at the ANTARES and IceCube sites, and can be used to send alerts to such telescopes. In ANTARES, the TAToO alert system shown in Fig. 30 has been running since 2009 [31].

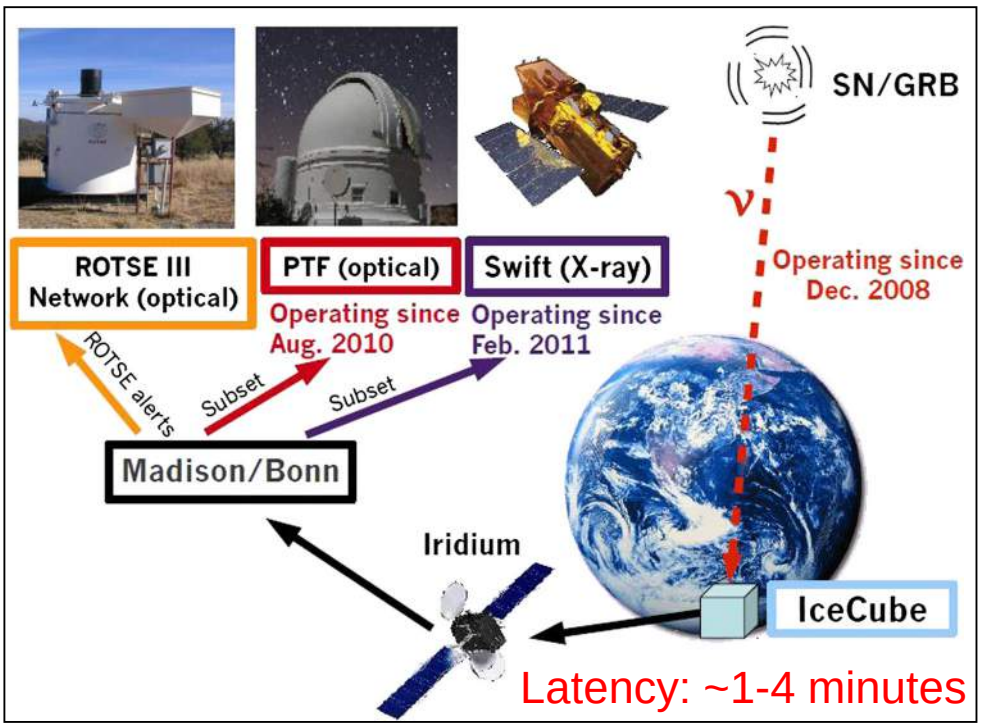

Fig. 31 Alert system at IceCube (from [32])

Table 2 Future high-energy neutrino detectors

Experiment: detector description	Reference
KM3NeT: $(km)^3$ water Cherenkov detector in the Mediterranean Sea	[34–39]
BAIKAL-GVD: $(km)^3$ water Cherenkov detector in Lake Baikal	[40]
ARA: $> 10 \times (km)^3$ detector with radio antenna array	[42–45]
ARIANNA: $> 10 \times (km)^3$ detector with radio antenna array	[46, 47]
ExaVolt Antenna (EVA) super balloon radio detector	[48]
Acoustic detector at ANTARES/KM3NeT	[49]
Earth-skimming tau neutrino shower detector (Ashra)	[50]
Radio detector on the moon surface	[51, 52]
Radio detector in a salt mine	[53]
Neutrino-initiated EAS by JEM-EUSO	[54]

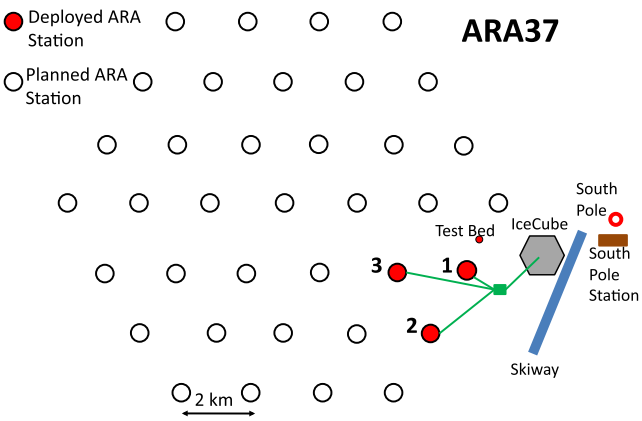

Fig. 33 Schematic view of ARA detector (from [42])

Neutrino events are selected based on either a coincidence of two or more events in terms of direction and time, a single very-high-energy event, or a single event whose direction is coincident with that of local galaxies. The parameters are tuned to achieve an alert rate of ∼2 alerts/month. The TAToO alert system can send an alert within 20 s and has an angular accuracy of 0.3–0.5 °. Figure 31 shows the alert system at IceCube [32]. Alerts are generated if two or more neutrinos are detected within 100 s of each other, and within 3.5 ° of each other. This program has been running since December 2008. Its latency for sending alerts is 1∼4 min. A similar alert system which sends alerts to Cherenkov high-energy gamma-ray telescopes (e.g., MAGIC and VERITAS) was reported in [33].

Although some astrophysical neutrinos have been detected at IceCube, to investigate the origin of high-energy neutrinos and the highest energy cosmic rays, many more such neutrino events are required. Table 2 shows a list of the future neutrino detectors discussed at ICRC2013.

KM3NeT is a multi-cubic-kilometer neutrino telescope in the Mediterranean Sea (Fig. 32).

Optimization of detector parameters such as inter-string and inter-DOM spacings, and deployment tests were reported in [34]. KM3NeT should be capable of detecting astrophysical neutrinos from RXJ1713.7-3946 and Vela X after about 3–5 years of observation. The BAIKAL-GVD neutrino project involves the construction of 2.0 km^3

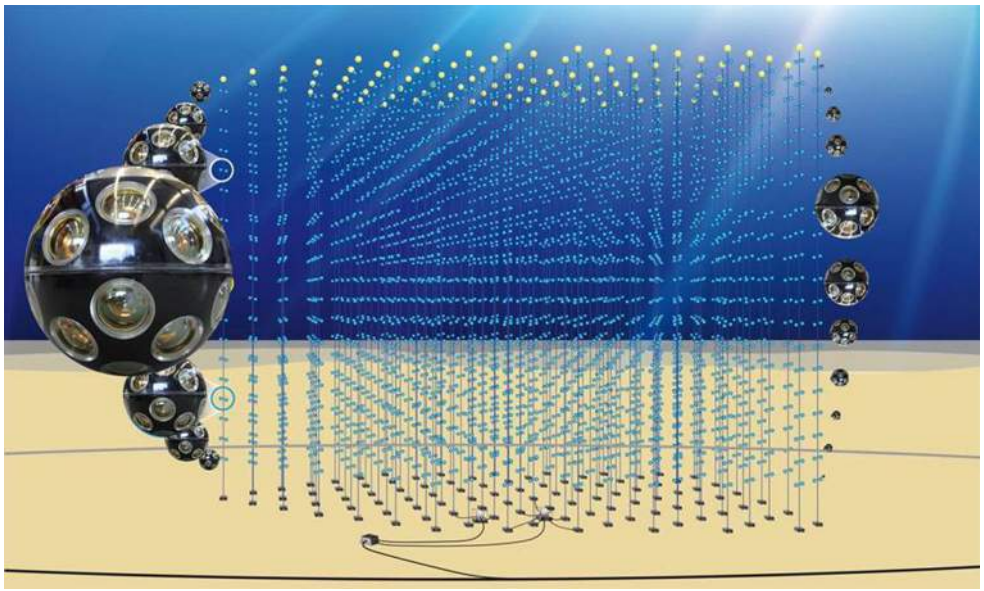

Fig. 32 Schematic view of the KM3NeT detector (from [34])

effective volume detector (at 1 PeV) in Lake Baikal. In April 2013, the pre-production version of an engineering array, comprising 72 optical modules, was deployed. The timeframe for construction is from 2014 to 2020.

At high energies (above 10^{16} eV), neutrinos can be detected in dense, radio-frequency transparent media via the Askaryan Effect [41]. The baseline design of the Askaryan Radio Array (ARA) involves 37 antenna clusters or "stations" arranged 2 km apart on a triangular grid, as shown in Fig. 33 near the IceCube site. Hardware prototyping has been completed and three stations are already operational [42], with three more planned for 2014–2015.

The ARIANNA (Antarctic Ross Iceshelf ANtenna Neutrino Array) is a surface array of radio receivers which detect signals reflected from the bottom of the Ice Shelf as shown in Fig. 34.

A prototype detector called Hexagonal Radio Array (HRA) has been installed and its pulse origin determination performance and angular resolution were described in [46]. The prototype detector is running well, and plans are in place to increase the number of detectors.

The sensitivity of the ARA and ARIANNA detectors is shown in Fig. 35. These detectors should be able to detect large numbers of GZK neutrino events.

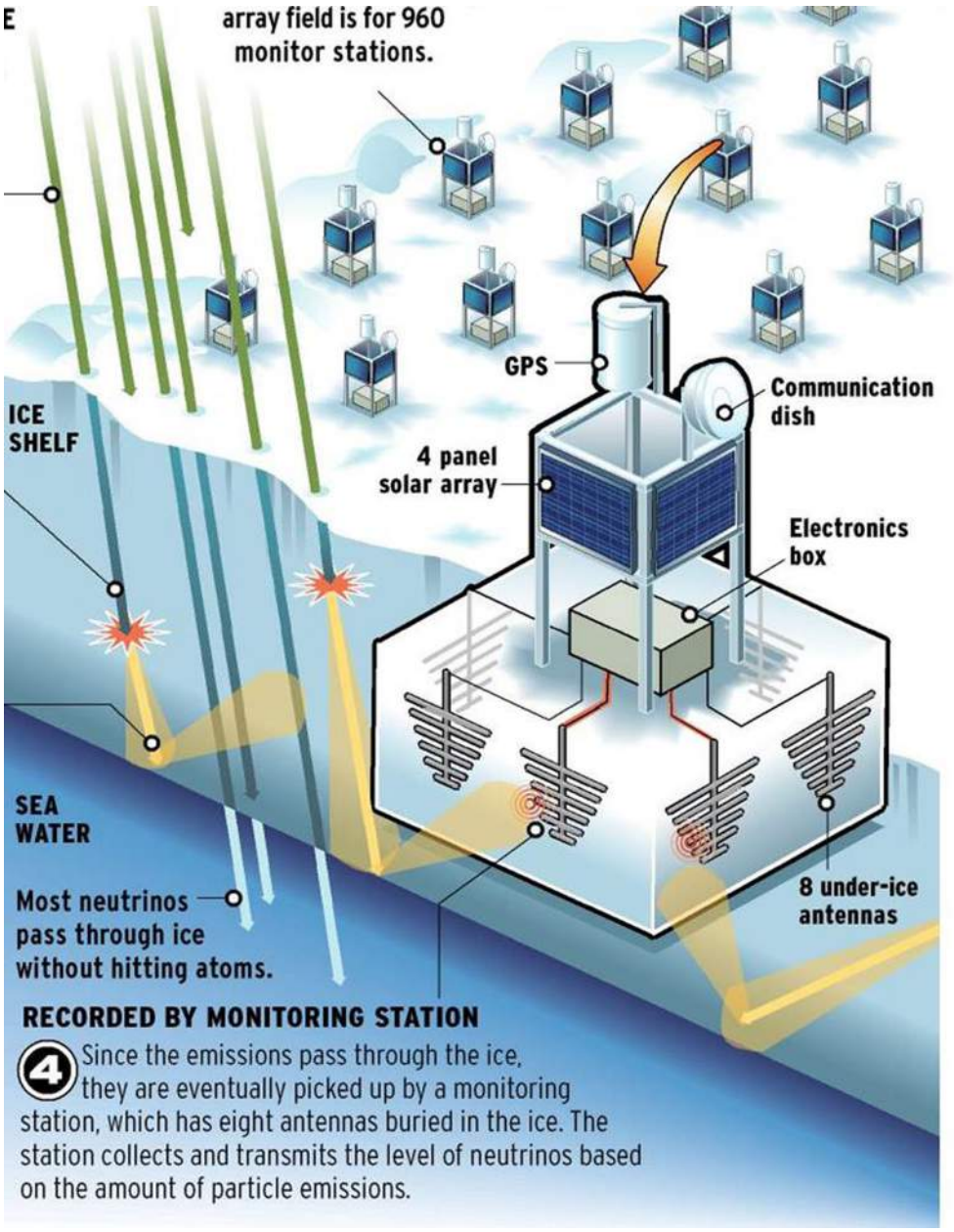

Fig. 34 Schematic view of the ARIANNA detector (from [46])

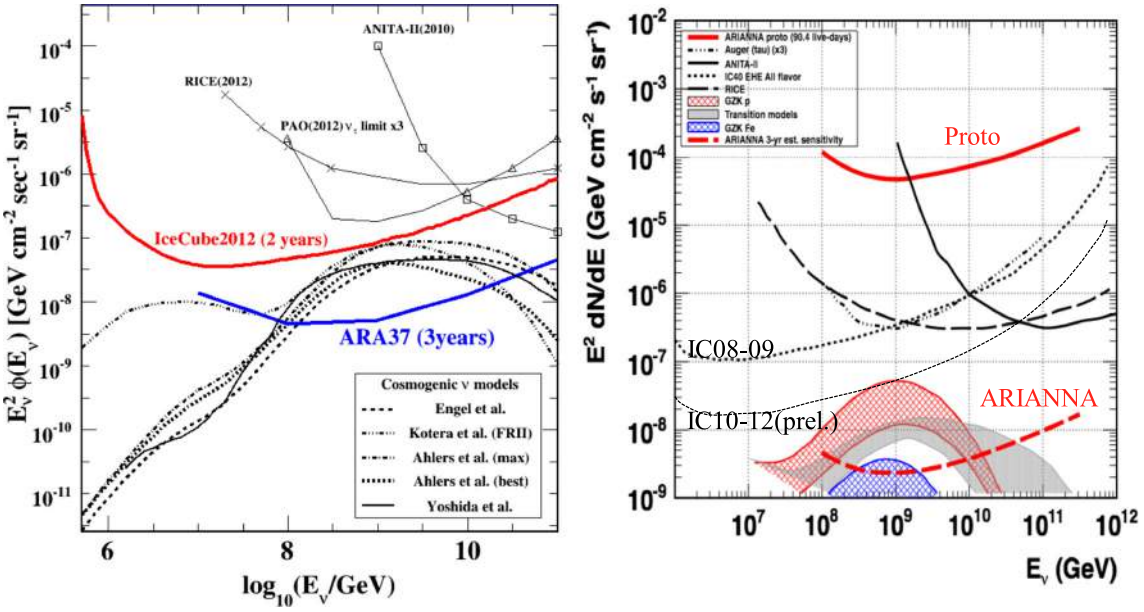

Fig. 35 Sensitivity of ARA and ARIANNA detectors

7 Conclusions

Neutrino related topics presented in NU-EX, NU-IN, and NU-TH categories have been reviewed. For solar neutrinos, a day/night difference due to the matter effect was indicated by Super-Kamiokande. Many detectors are waiting for the occurrence of the next galactic supernova, and fruitful measurements are expected. Results obtained from supernova detectors already in long-term operation have allowed an upper limit to be placed on the galactic supernova rate. Atmospheric neutrinos have provided a large amount of information on neutrino oscillations, and the mass hierarchy may be determined in the future by high statistical observations of atmospheric neutrinos. Many results from the IceCube and ANTARES experiments were presented at this conference. In particular, evidence for high-energy extraterrestrial neutrinos was obtained at IceCube using cascade events. Future progress with regard to astrophysical neutrinos is also expected.

References

1. K. Abe et al., (T2K collaboration), arXiv: 1308.0465[hep-ex]
2. H. Sekiya et al., (Super-Kamiokande collaboration), ICRC2013 presentation, ID:48
3. A. Gaponenko et al., ICRC2013 presentation, ID:621
4. C. Vigorito et al., (LVD collaboration), ICRC2013 presentation, ID:453
5. G. Kroll et al., (IceCube collaboration), ICRC2013 presentation, ID:446
6. D. Heereman et al., (IceCube collaboration), ICRC2013 presentation, ID:444
7. L. Marti et al., (Super-Kamiokande collaboration), ICRC2013 presentation, ID:719
8. M. Medeiros et al., (MINOS collaboration), ICRC2013 presentation, ID:958
9. C. Wiebussh et al., (IceCube/DeepCore collaboration), ICRC2013 presentation, ID:848
10. J.P. Yanez et al., (IceCube/DeepCore collaboration), ICRC2013 presentation, ID:450
11. A. Gross et al., (IceCube collaboration), ICRC2013 presentation, ID:555
12. M. Honda et al., ICRC2013 presentation, ID:990
13. P. Desiati et al., (IceCube collaboration), ICRC2013 presentation, ID:492
14. T.K. Gaisser et al., ICRC2013 presentation, ID:1144
15. T.S. Sinegovsky et al., ICRC2013 presentation, ID:0040
16. C. Kopper et al., (IceCube collaboration), ICRC2013 presentation, ID:650
17. M. Richman et al., (IceCube collaboration), ICRC2013 presentation, ID:1180
18. C.W. James et al., (ANTARES collaboration), ICRC2013 presentation, ID:760
19. J.A. Aguilar et al., (IceCube collaboration), ICRC2013 presentation, ID:550
20. S. Schulte et al., (ANTARES collaboration), ICRC2013 presentation, ID:425
21. A. Bernhard et al. (IceCube collaboration), ICRC2013 presentation, ID:471.
22. A. Cruz et al., (IceCube collaboration), ICRC2013 presentation, ID:539
23. J. Aguilar et al., (IceCube collaboration), ICRC2013 presentation, ID:649
24. T. Pradier et al., (ANTARES collaboration), ICRC2013 presentation, ID:778
25. D. Dormic et al., (ANTARES collaboration), ICRC2013 presentation, ID:296
26. V. Kulikovskiy et al., (ANTARES collaboration), ICRC2013 presentation, ID:031
27. S. Mangano et al., (ANTARES collaboration), ICRC2013 presentation, ID:614

28. F. Schussler et al., (ANTARES collaboration), ICRC2013 presentation, ID:420
29. D. Xu et al., (IceCube collaboration), ICRC2013 presentation, ID:643
30. J. Kiryluk et al., (IceCube collaboration), ICRC2013 presentation, ID:494
31. D. Dornic et al., (ANTARES collaboration), ICRC2013 presentation, ID:299
32. M. Voge et al., (IceCube collaboration), ICRC2013 presentation, ID:852
33. D. Gora et al., (IceCube collaboration), ICRC2013 presentation, ID:537
34. M. De Jong, ICRC2013 presentation, ID:891
35. A. Trovato et al., (KM3NeT collaboration), ICRC2013 presentation, ID:165
36. R. Coniglione et al., (KM3NeT collaboration), ICRC2013 presentation, ID:1249
37. S. Henry et al., (KM3NeT collaboration), ICRC2013 presentation, ID:1163
38. M. Circella et al., (KM3NeT collaboration), ICRC2013 presentation, ID:1222
39. P. Kooijman et al., (KM3NeT collaboration), ICRC2013 presentation, ID:164
40. A.V. Avrorin et al., (BAIKAL collaboration), ICRC2013 presentation, ID:510
41. G.A. Askaryan, JETP **14**, 441 (1962)
42. K.D. Hoffman et al., (ARA collaboration), ICRC2013 presentation, ID:704
43. C.G. Pfendner et al., (ARA collaboration), ICRC2013 presentation, ID:1230
44. T. Meures et al., (ARA collaboration), ICRC2013 presentation, ID:162
45. E.S. Hong et al., (ARA collaboration), ICRC2013 presentation, ID:1161
46. S.W. Barwick et al., (ARIANNA collaboration), ICRC2013 presentation, ID:825
47. C. Reed et al., (ARIANNA collaboration), ICRC2013 presentation, ID:834
48. A. Connolly et al., (EVA collaboration), ICRC2013 presentation, ID:1152
49. R. Lahmann et al., (ANTARES collaboration), ICRC2013 presentation, ID:745
50. Y. Aita et al., (ASHRA-1 collaboration), ICRC2013 presentation, ID:977
51. A. Aminaei et al., ICRC2013 presentation, ID:223
52. C.W. James, ICRC2013 presentation, ID:1052
53. A.M. Badescu et al., ICRC2013 presentation, ID:232
54. Alejandro Guzmán et al., (JEM-EUSO collaboration), ICRC2013 presentation, ID:533